Microstructure and gas-surface interaction studies of a 3D carbon/carbon composite in atmospheric entry plasma

C. Levet, B. Helber, J. Couzi, J. Mathiaud, J.-B. Gouriet, O. Chazot, G. Vignoles

Microstructure and gas-surface interaction studies of a 3D carbon/carbon composite in atmospheric entry plasma

C. Levet[a,b], B. Helber[c], J. Couzi[b], J. Mathiaud[b], J.-B. Gouriet[c], O. Chazot[c], G. L Vignoles[a,*]

[a] *University of Bordeaux, LCTS, 3 allée de la Boétie, F-33600 Pessac, France*
[b] *CEA,CESTA, 15 Avenue des Sablières, 33114 Le Barp, France*
[c] *von Karman Institute for Fluid Dynamics, Chaussée de Waterloo 72, B-1640 Rhode-Saint-Genèse, Belgium*

Abstract

3D Carbon-fiber reinforced carbon composites (3D C_f/C) are widely used as thermostructural protections in various applications. Among them, thermal protection systems for atmospheric re-entry encounter one of the most aggressive environments, where 3D C_f/C are exposed to strong ablation. Because flight tests are extremely expensive, Inductively Coupled Plasma torch is a good compromise to understand the behaviour of this material under ablative conditions. The Plasmatron of the von Karman Institute for Fluid Dynamics is used in this study, coupled with a numerical rebuilding of the flow. Air and argon flows are used on flat and hemispherical 3D C_f/C samples leading to surface temperatures ranging from 1800 °C to 2500 °C. *In-situ* measurements are performed coupled with SEM micrography and 3D pictures from digital optical microscopy in order to understand the epi-macro-structural and the epi-micro-structural roughness of the composite. The internal structure of the composite was revealed by the differences in ablation

*Corresponding author. E-mail: vinhola@lcts.u-bordeaux.fr

resistance between constituents. It is found that the flow field has a major contribution to the composite macroscopic and mesoscopic roughness and recession velocity.

Nomenclature

Acronymes

HB	Horizontal Bundle
HS	Hemispherical
MO	Matrix Octet
ST	Standard
VB	Vertical Bundle

Indices et exposants

d	Dynamic
dl	Diffusion-limited values
e	Boundary layer edge
eff	Effective value
exp	Experimental values
f	Flight quantity
i, j	Chemical species indices

s Static

t Test quantity

Variables

β Radial velocity gradient at the wall, s^{-1}

δ Boundary layer thickness, mm

ϵ Emissivity

ρ Sample density, kg m^{-3}

σ Standard deviation

τ Sample exposure time, s

υ Molar volume of solid, m^3 mol^{-1}

χ Mole fraction

C Gaseous species concentration, mol m^{-3}

D Diffusivity, m^2 s^{-1}

$D_{i,j}$ Mutual diffusion coefficient, m^2 s^{-1}

h Total enthalpy, J

k Heterogeneous reaction rate, m s^{-1}

M_s Molar mass of the solid, kg mol^{-1}

nb Number of measurements points

p Pressure, Pa

$Pé$ Péclet number

q_{cw} Cold wall stagnation point heat flux, W m^{-2}

$\dot{r}$ Sample recession rate, µm s^{-1}

$\tilde{\dot{r}}$ Dimensionless recession rate

R_f Fiber radius, m

Sh_f Fiber Sherwood number

T Temperature, K

u Flow axial velocity, m s^{-1}

v Flow radial velocity, m s^{-1}

y Radial coordinate, m

1. Introduction

Carbon-fiber reinforced carbon composites (CFRC, CFC, Carbon/Carbon or C_f/C for short) are dedicated to high technology structural and thermal applications in aggressive environments [1]. They are used as thermostructural protections in various applications such as atmospheric re-entry [2, 3], rocket propulsion [4, 5], aircraft braking systems [6] and plasma facing elements of the Tokamak [7, 8]. In the first two applications, the C_f/C composites are progressively destroyed by oxidation, nitridation, sublimation, and, up to a certain extent, thermomechanical erosion. These phenomena are collected in the generic term of ablation. They are usually globally endothermic, transforming the thermal energy into

mass loss and surface recession, whilst the remaining solid material insulates the vehicle substructure [9].

Selection and thickness definition of the Thermal Protection Material (TPM) are key performance parameters in Thermal Protection System (TPS) design. Prediction inaccuracies can be fatal for the re-entry vehicle. However, the complex behavior of C_f/C composites is not fully understood, and currently not accurately accounted for in the models. Ablation of C_f/C composites is known to lead, among others, to a typical surface roughness [10, 11]. The surface roughening, which is inseparable from material behavior and flow field, contributes to the laminar-to-turbulent transition of the boundary layer [12, 13]. The PAssive Nosetip Technology (PANT) program results have shown that the heat flux can be multiplied by a factor of up to three in turbulent regime[14]. Therefore, the understanding of the interaction between the material and its close environment has to be improved for all of these applications.

Consequently, ground testing becomes a fundamental requirement for TPM qualification, validation of material response code and TPS design. Plasma windtunnels are among the most interesting facilities in this aim. In this work, we report new data to improve the understanding of the behavior of dense C_f/C composites during atmospheric re-entry and to feed multi-scale models of ablation. In order to reproduce the aero-thermodynamic environment of atmospheric entry in the boundary layer, the subsonic 1.2 MW Inductively Coupled Plasma (ICP) torch of the Plasmatron facility of the von Karman Institute (VKI) has been used. It allows the use of a wide range of pressures and heat fluxes [15, 16]. An extensive numerical rebuilding procedure offers a detailed characterization of the flow.

Flat and hemispherical samples were tested at pressures of 1.5 – 20 kPa, heat

fluxes of $734 - 2861$ kW/m^2 and surface temperature of $1800 - 2500$ °C. This paper will first describe the experimental and characterization facilities; then, the experimental results will be exposed. In the last section, consequences of the results for a modeling strategy will be discussed.

2. Experimental techniques

2.1. Test material

The material was a 3D C_f/C composite made from ex-PAN carbon fibers and an ex-pitch carbon matrix [10]. Several thousands of fibers are linked together by a pitch-based matrix in a straight, unidirectional yarn, named "bundle". Then, fiber bundles are fit together into a 3D orthogonal pattern repeated by translation of a cubic lattice. This leads to a network of parallelepipedic macropores, hereafter named "octets". They are partially filled with a pitch-based carbon matrix. Finally, the composite is graphitized.

Two different sample shapes, schematized in figure 1, were used in these tests. The first ones were flat samples which were used for stagnation point characterization tests. They are 4 mm thick and have a radius of 25 mm. They will be called Standard samples (*ST*) in the following. The second ones were hemispherical samples (*HS*). They have a radius of 15 mm and a 34 mm length. They were used for stagnation point and off-stagnation point tests.

Standard samples were held by a graphite cap and attached to a cooled sample holder (Figure 1a)). Hemispherical samples were only attached to the sample holder (Figure 1b)). A 0.1 mg precision balance was used for pre- and post-test

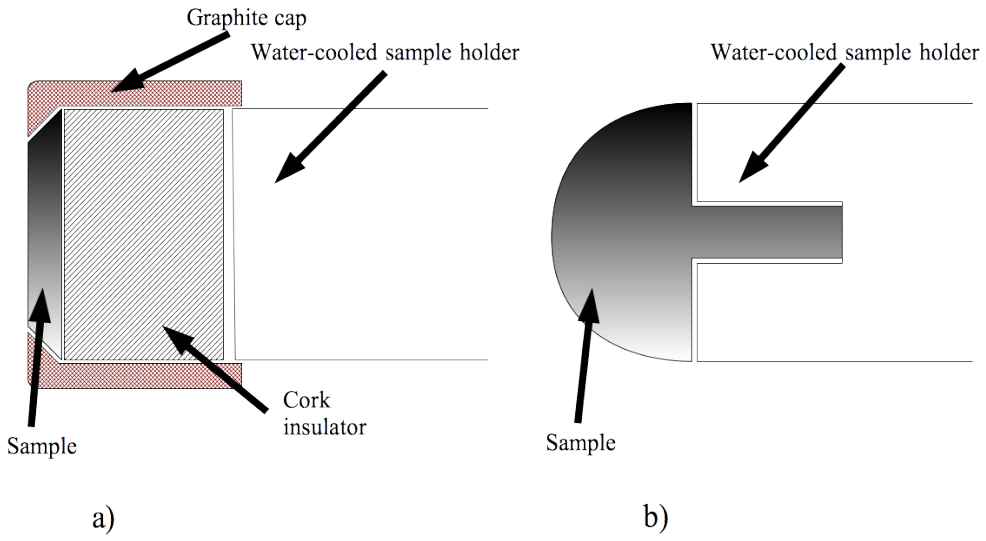

Figure 1: Scheme of the assembly of a) flat and b) hemispherical samples for the VKI Plasmatron experiments.

evaluation of mass loss of samples. All samples surfaces were polished to under .5 μm precision before the tests.

2.2. Plasma wind tunnel overview

The VKI Plasmatron has been used for all the experiments. It has the ability to reproduce the aero-thermodynamic environment of re-entry plasma flows, creating a high-enthalpy, highly dissociated subsonic gas flow. The Plasmatron is equipped with a 160 mm diameter ICP torch powered by a high frequency (400 kHz), high power (1.2 MW), high voltage (2 kV) generator (with Complementary Metal-Oxide-Semiconductor (CMOS) technology). The gas is heated by

induction through a coil, creating a high purity plasma flow [15].

A schematic of the experimental setup for *in-situ* ablation measurement can be found in figure 2. Surface temperature measurements were carried out using a bichromatic Raytek Marathon MR1S-C pyrometer (0.75 – 1.1 μm), with a temperature range from 1300 K to 3300 K. A KT19 Heitronics Infrarot Messtechnik GmbH radiometer was used for emissivity checking and temperature measurement for sublimation tests. The emissivity of the material is $\epsilon = 0.89$. It was determined from *in-situ* measurements combining the radiometer (broad wavelength, emissivity dependant) and the bichromatic pyrometer (surface temperature, emissivity independant). The temperature in the case of argon flow was obtained from the radiometer data. Surface recession was recorded *in situ* with a Vision Research 7.1 High-Speed Camera (HSC). Identification of ablation products can be carried out using a low-resolution Ocean Optics HR4000 spectrometer.

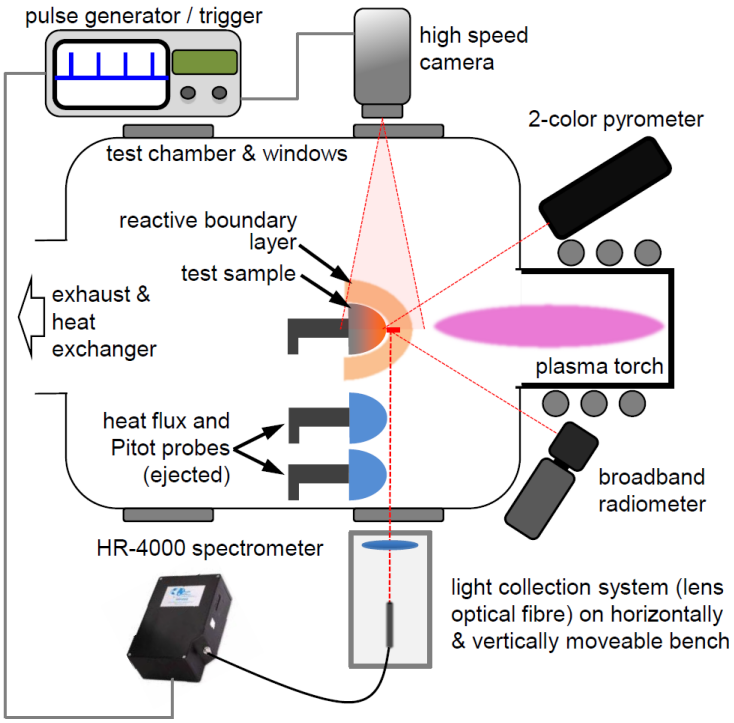

Figure 2: Plasmatron set-up for in-situ measurement for hemispherical samples

2.2.1. Plasma flow characterization by intrusive probes

The cold wall (~350 K) stagnation point heat flux $\dot{q}_{cw}$ was measured with a flat water-cooled calorimeter made of copper. Additionally, a probe with the same shape as the test sample was used for tests with *HS* samples. A calibrated rotameter served to determine the water mass flow, and inlet/outlet temperatures were measured by two type-E thermocouples. A Teflon® insulator was inserted between calorimeter and probe holder to achieve adiabatic conditions at the calorimeter wall. The uncertainty on the heat flux measurement was estimated to be about ±10% [16]. Determination of the dynamic pressure of the flow was achieved by using a water-cooled Pitot probe, connected to a Validyne variable reluctance pressure transducer. The output voltage was amplified by a voltage demodulator. Both of them were calibrated prior to the tests by a Betz water manometer. The test chamber is also equipped with an absolute pressure transducer to measure the static pressure with an accuracy of ± 2 Pa.

Before the injection of the sample, the generator power was adjusted to calibrate the target wall heat flux. The cold wall heat flux was measured by the calorimeter and the generator power was modified in order to adjust the plasma jet energy. After withdrawing the sample, whenever possible, the calorimeter was injected a second time to control the stability of the heat flux. Table 1 shows that the heat flux variation has been in the calorimeter measurement error except for the low flux test (*Long Duration ST*) where a 15% variation of the heat flux can be noticed.

Test	$\dot{q}_{cw}$(MW m^{-2}) before	$\dot{q}_{cw}$(MW m^{-2}) after	$\Delta q_{cw}/q_{cw}$
Reference ST	1.012	1.020	+0.79 %
Long Duration ST	0.734	0.687	-15%
Oxidation ST	1.914	1.747	-9.6%
Sublimation ST	1.766	1.630	-8.3%

Table 1: Cold wall heat flux, $\dot{q}_{cw}$, before and after the ablation test and relative variation of this flux.

2.2.2. Computation of the plasma free-stream composition

Duplication of the hypersonic entry condition in a ground-test plasma facility can be achieved under the Local Thermochemical Equilibrium (LTE) assumption if the boundary layer edge total enthalpy h_e, total pressure p_e and the radial velocity gradient at the wall β_e are locally matched on the test sample [17]:

$$h_e^f = h_e^t \quad p_e^f = p_e^t \quad \beta_e^f = \beta_e^t \tag{1}$$

f and t stand for "flight" and "test" quantities, respectively. $\beta_e = \frac{\partial v}{\partial x}|_e$ with x and v which are the axial coordinate and the radial velocity.

The subsonic Plasmatron flowfield is numerically simulated using a Navier-Stokes equation solver, characterizing the boundary layer geometry around the test sample under LTE and axisymmetric flow assumptions This assumption is made by the VKI ICP code and, even if not totally correct for our studies, sufficient to obtain good agreement. [18, 19, 20]).

The boundary layer is thermally defined by:

$$h <= 0.95 h_{\text{inf}} \tag{2}$$

where h_{inf} is the total enthalpy of the free flow. The code makes use of the **Mutation^{++}** library [21] to determine thermodynamic and transport properties of an air mixture composed by eleven species : O_2, N_2, O_2^+,N_2^+, NO, NO^+, O, O^+,

N^+, N and e^-. The temperature of the sample surface is fixed and the input power is chosen in order to match experimental heat flux on the sample.
The main output data of this simulation are the size of the boundary layer and the physical values (velocity, temperature, species fractions, ...) at the boundary layer outer edge.

2.3. High-speed camera application for in situ *surface recession determination*

It is not easy to measure surface recession of an ablating test sample. Because meso- and micro-structural roughness is a main concern of this study, caliper rule measurement is not advised. Indeed, making use of a caliper rule can destroy the fragile meso-structures of the 3D C_f/C roughness features. A Vision Research Phantom 7.1 CMOS high-speed camera (HSC) with a short exposure time (2 µs) has been used for in situ recession analysis of the ablating test samples. The short exposure time prevents CCD sensor saturation. The determination of the recession rate from HSC data was only available for hemispherical samples, because the camera axis needs to lie perpendicular to the sample axis. Due to the camera resolution, which is 126 µm by pixel, only the overall recession rate was accessible, by making the difference between the first and the last image taken by the camera.

(deleted subsection)

2.4. Material characterization

Morphological characterization was performed by Scanning Electron Microscopy (SEM), and by confocal and 3D optical microscopy. The SEM system used in this study was an FEI Quanta 400 FEG environmental SEM. The accelerating voltage was 5 kV and the working distance varied between 10 mm and 60 mm. Confocal microscopy was made using a Sensofar S-NEOX confocal microscope.

$4 \times 3\,mm^2$ and $13 \times 5\,mm^2$ pictures were taken with this microscope.

The second 3D optical microscope is a Keyence VHX-2000. Its large depth of field allows a 3D reconstruction of the sample surface and therefore gives access to composite roughness measurements. The focus of the microscope was set on the sample holder, then it was shifted to the top of the sample and the microscope software measured the distance between the two positions. This method was applied to all samples and to two non ablated samples for sake of reference. The recession rate was obtained by calculating the height difference between ablated and non ablated samples and dividing by the test time. Because this method depends on the chosen point on the sample surface, nine measurements were taken for each sample. The standard deviation was always less than 1% of the mean value.

3. Results

The test conditions of material ablation are summarized in table 2. Two geometries were used : Standard samples for stagnation point experiments and hemispherical samples for comparison between stagnation and off-stagnation points. The target temperatures were 1800 °C and 2500 °C. A first experiment with a heat flux of 1 MW m^{-2} was performed in order to match previous works [11]. The tests were carried out with air or pure argon, the latter experiments in order to quantify the sublimation rate in ablation process. The static pressure was held at 200 mbar for air tests and 15 mbar for argon tests. In these conditions, the stability of the jet was ensured. The gas mass flow was 16 g/s for test under air and 8 g/s for sublimation tests, and the test time was 180 s for all tests except one where a 300 s test was performed to ensure stationary ablation. Linear recession

rate are also included in table 2. Figure 3 shows a picture of the *Oxidation HS* sample before and after plasma exposure.

Sample	Geometry	Gas	p_s (kPa)	p_d (Pa)	$\dot{q}_{ch}$ (MW.m^{-2})	T_s (K)	τ (s)	$\dot{r}$ (μm.s^{-1})
Reference ST	Standard	Air	20	16.9	1.020	2303	180	4.43
Oxidation ST	Standard	Air	20	65.0	2.345	2806	180	6.16
Long Duration ST	Standard	Air	20	11.3	0.687	2073	300	3.87
Sublimation ST	Standard	Ar	1.5	421	1.136	2394	145	0.08
Oxidation HS	Hemispherical	Air	20	36	2.861	2779	180	10.24
Sublimation HS	Hemispherical	Ar	1.5	372	1.630	2426	180	< 0.6

Table 2: Plasmatron test conditions : test case name, sample geometry, test gas, static pressure p_s, dynamic pressure p_d, cold wall heat flux $\dot{q}_{ch}$, mean surface temperature T_s, sample exposure time τ, and recession rate $\dot{r}$

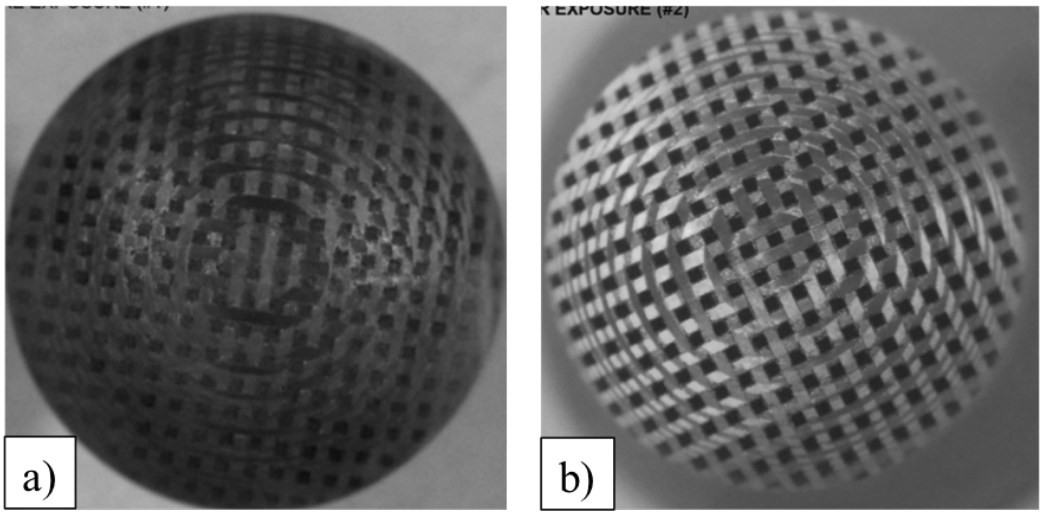

Figure 3: Micrographs of the *Oxidation HS* sample before (a) and after (b) ablation on the Plasmatron

From the numerical rebuilding of the plasma free-stream composition, we ob-

tained the boundary layer size, the flow axial velocity u_e, the temperature T_e and the partial pressure of air components at the outer edge of the boundary layer on the stagnation line as listed in table 3 for all tests under air flow and one test under argon flow. For the other one (*Sublimation ST*), numerical convergence could not be attained. An example of the simulated flow field for the *Oxidation HS* experiment can be found on figure 4.

Sample	δ (mm)	u_e (m s^{-1})	T_e (K)	Partial pressures $p_{e,i}$ (Pa)						
				O	O^+	O_2	N	N^+	N_2	NO
Reference ST	10	93.2	7258	4402	6.09	$6.85 \cdot 10^{-2}$	14518	23.66	1014	7.96
Oxidation ST	10	156	10158	3779	174.6	$4.24 \cdot 10^{-3}$	13848	1007	7.23	0.24
Long Duration ST	7.3	61.8	6497	4814	2.094	0.24	10966	2.946	3980	25.3
Sublimation ST	9	46.1	10666	-	-	-	-	-	-	-
Oxidation HS	6.5	168	9646	4009	82.27	$8.34 \cdot 10^{-3}$	14888	455	25.36	0.59

Table 3: Numerical boundary layer edge characterization for air and argon plasma : boundary layer size δ, axial velocity u_e, temperature T_e and partial pressures p_e of the air species.

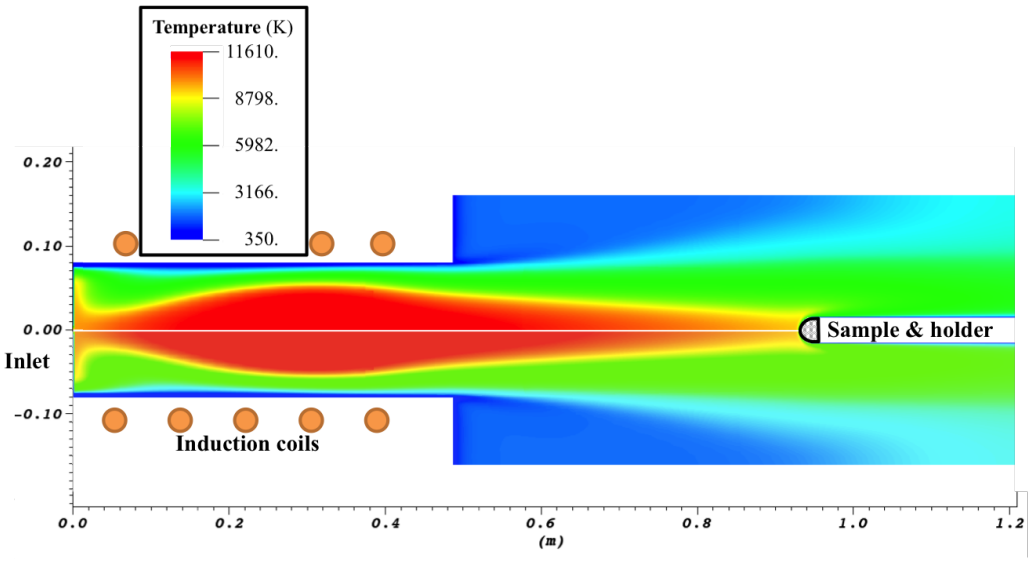

Figure 4: Temperature field of an axisymetrical equilibrium computation of the flow inside the Plasmatron ICP torch and test chamber including a hemispherical test sample for test *Oxidation HS*. The sample surface thermal boundary condition is a cold wall boundary condition.

		All values in μm.s^{-1}			
Sample	HSC	3D microscopy	Weighing	Retained $\dot{r}$	Uncertainty
Reference ST	-	4.66	4.2	4.43	0.3
Oxidation ST	-	6.21	6.1	6.16	0.06
Long Duration ST	-	3.94	3.8	3.87	0.07
Sublimation ST	-	0.08	≈ 0.13	0.08	-
Oxidation HS	5.4	9.61	15.7	9.61	4.2
Sublimation HS	< 0.6	-	0.2	< 0.6	-

Table 4: Recession rate of samples according to HSC data, 3D digital microscopy data and mass loss data

3.1. Recession of the samples

Recession data are presented in table 4. Because the recession of the samples was weak, three methods were used to calculate it. The first was HSC recording and has severe limitations: (*i*) data is available only for *HS* samples, and (*ii*) only the overall rate (*i.e.* between the first and last frame of the movie) can be measured. This induces another limitation of the method which is the assumed hypothesis that the transient phase of the ablation test has been negligible compared to the stationary one. Owing to the long duration of the tests (at least 180 s) and the high surface temperatures reached during the experiments, this hypothesis is not too strong. However, a slight under-estimation of the actual ablation rate is expected. Moreover, the recession rate of the sample *Sublimation HS* was too slow to be measured by this method: we could only determine an upper bound for it. The second method based on the digital 3D microscope, proved much more efficient; however it failed to provide a value for the hemispherical sample under argon, because of its very low recession rate. The third method, based on

mass loss measurements, has important potential drawbacks. First, the mass of the samples can significantly change with sample manipulation and ambient humidity variations. Nevertheless, it can be used for comparison when one of the first two methods cannot be used. With our dense sample ($\rho \approx 2g.cm^{-3}$), the mass gain with ambient moisture is negligible, so the weighing agrees with 3D microscopy for *ST* samples (see table 4). On the other hand, for *HS* samples, a hypothesis of uniform ablation across the whole surface was made to calculate the recession rate from mass loss data. Unfortunately, this hypothesis is not verified, inducing a discrepancy with respect to HSC data.

Finally, in table 4, a retained value is provided for the linear recession rate $\dot{r}$, which is the Keyence measurement data because they are available for all the test samples and more accurate than others measurements. From this table, it is obvious that at temperatures lower than 2500 K, sublimation plays only a minor role on the ablation of 3D C_f/C composites. When it is measurable, the ablation rate in argon flow is nearly an hundred times lower than in air flow.

For *ST* samples ablated under air flow, the ablation rate increases with temperature. It is more difficult to compare with sample *Oxidation HS* because its ablation rate has been determined with less precision, but it seems to increase with the heat flux.

3.2. Surface morphology characterization

Figure 5 presents micrographs of the samples tested . Samples ablated under air (Figures 5(a), 5(b), 5(f) and 5(d)) show deep ridges between fiber bundles and matrix. They arise from recession of the thin interface between octets and fiber bundles and are a commonly reported pattern in oxidation of C_f/C composites [9]. On the contrary, the less disturbed surface obtained under argon (Fig-

ures 5(c) and 5(f)) as compared to the oxidative cases confirmed that sublimation was very low under argon flow.

Figure 6 presents micrographs of fibers located in bundles perpendicular to the surface of the sample for three locations in *Oxidation HS* sample and for *Oxidation ST* sample. A scheme of the locations is presented on Figure 6(a). All the conditions give similar morphologies. Fibers and intra-bundle matrix acquire a needle shape due to recession of a thin, less organized, more reactive carbon layer [22, 23, 24, 25, 26]. More precisely, as shown on figure 6(b), the fibers internal organization appears with a core, which is more resistant to ablation than an intermediate zone, and a thin skin; the fibers tip is nearly flat. On the other hand, on figure 6(c), 6(d) and 6(e), the internal structure of fibers is less perceptible, whereas a needle shape is more strongly marked. Moreover, if the *center* and *middle* fibers are very similar, the matrix has been less ablated on the edge of the sample. This is consistent with a smaller ablation rate caused by the smaller temperature at the edge of the hemispherical sample.

Under argon flow the intra-bundle matrix surface lies above the fibers instead of below (see Figure 7). This "reverted" behaviour agrees with previous studies [27, 9]. The differences between flat and hemispherical samples will be discussed in 4.2.

Matrix and horizontal fibers ablation patterns are presented in figure 8. All are SEM micrographs of samples after an ablation test under air flow. Samples ablated under argon present the same structures, though less visible due to very weak recession. The highly graphitized matrix presents carbon sheets mostly oriented perpendicularly to the surface sample. Moreover, ablation uncovered pores inside

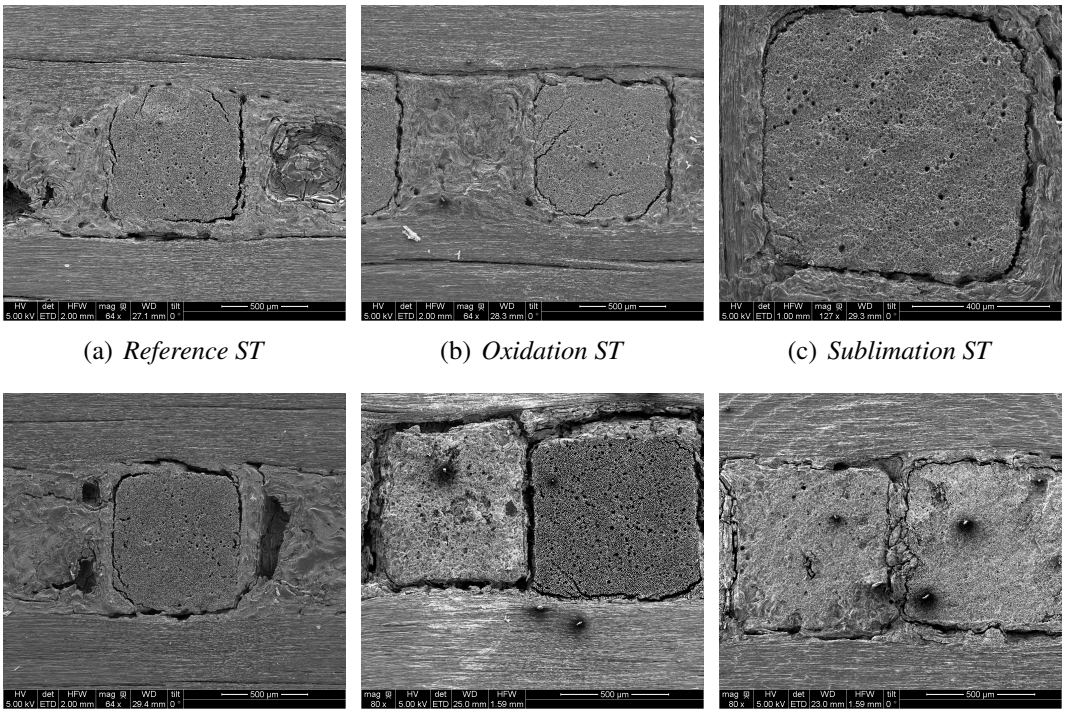

(a) *Reference ST* (b) *Oxidation ST* (c) *Sublimation ST*

(d) *Long Duration ST* (e) *Oxidation HS* (f) *Sublimation HS*

Figure 5: SEM micrographs of C_f/C composites ablated at the VKI Plasmatron.

the matrix. Even if the 3D C_f/C contains a very low pore volume fraction, these pores can play a role in ablation at mesoscopic scale by increasing the ablation rate of the matrix. Fibers in horizontal bundles are completely denuded, because the matrix has been removed in more depth, and have a blade-like shape with scallops.

Ridges around the fibers bundles and the octets come from the important recession of the less organized carbon interface. Nonetheless, these cracks do not perfectly follow the composite pattern. Some fibers can be separated from the bundle or, conversely, matrix can remain stuck on bundles because of pre-existing cracks or

defects (see figure 5).

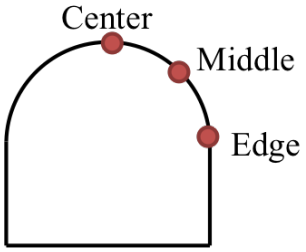

(a) Scheme of HS sample locations

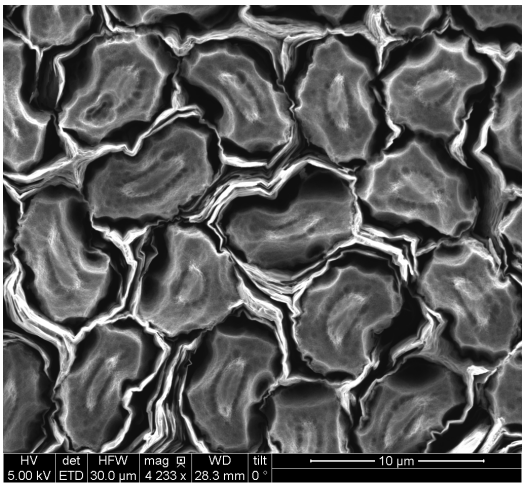

(b) *Oxidation ST*

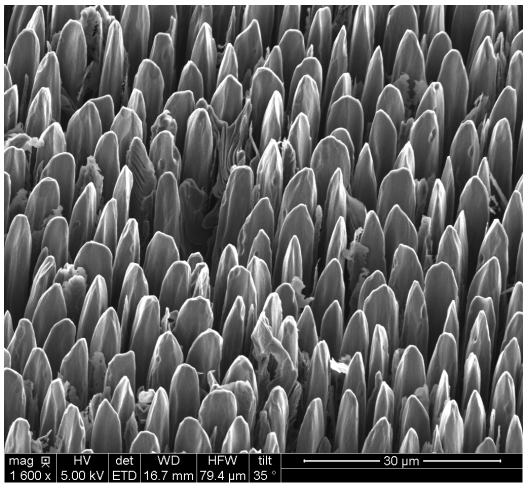

(c) *Oxidation HS center*

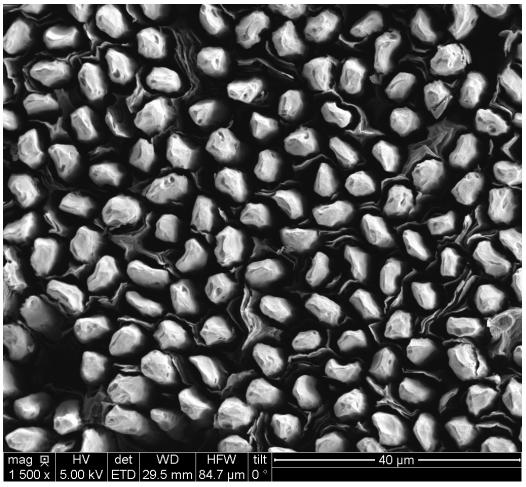

(d) *Oxidation HS middle*

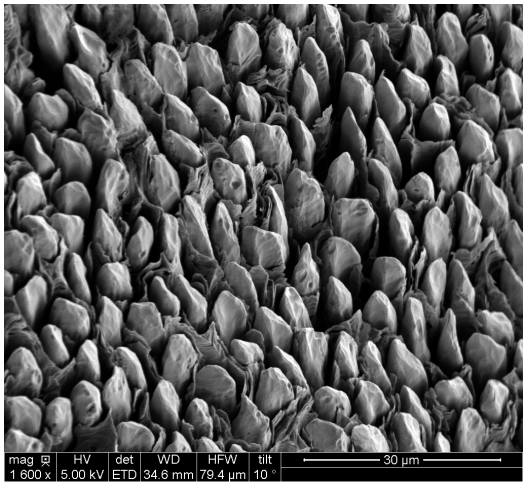

(e) *Oxidation HS edge*

Figure 6: SEM pictures of fiber bundles perpendicular to the surface for *ST* and *HS* samples ablated under air. A scheme of the observations locations on HS samples is presented in a).

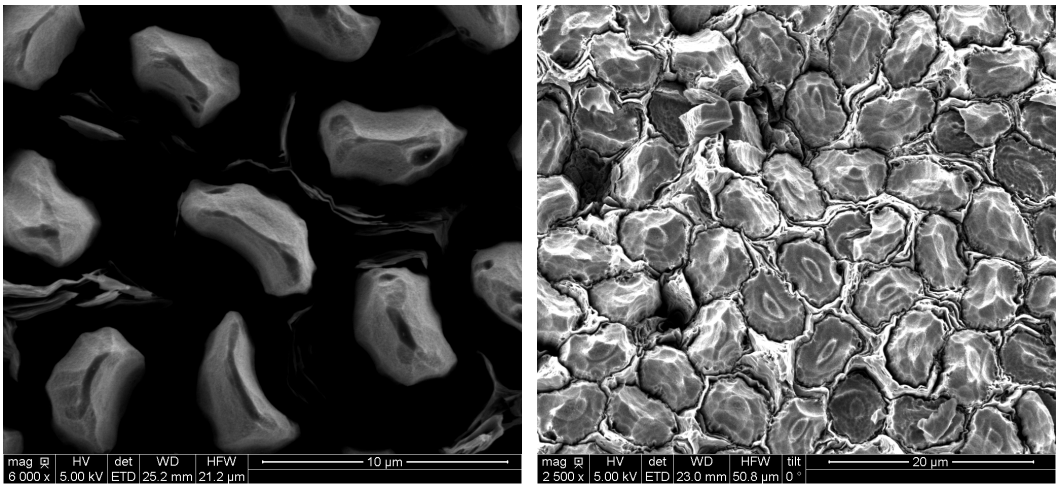

(a) HS sample ablated under air

(b) HS sample ablated under argon

Figure 7: SEM pictures of fiber bundles perpendicular to the flow for *HS* samples at the stagnation point ablated under air and argon flow.

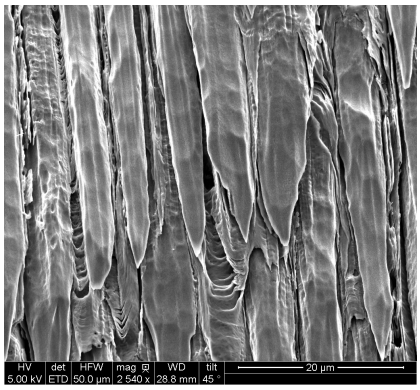

(a) Horizontal fiber bundle of *Reference ST*

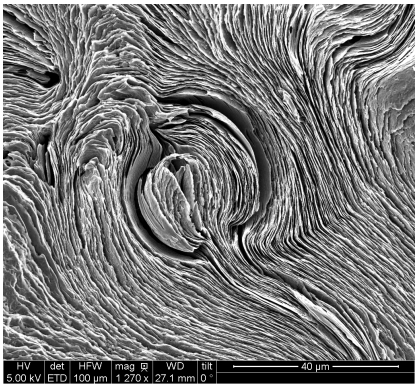

(b) Matrix octet of *Reference ST*

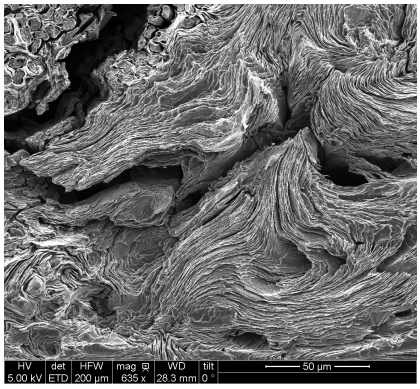

(c) Matrix octet of *Oxidation ST*

Figure 8: SEM pictures of horizontal fibers bundle and matrix octets for standard samples ablated under air flow.

3.3. Quantitative morphological data

By confocal microscopy, quantitative depth profiles were obtained. For example, Figure 9 shows a 2D depth map of the surface of the *Reference ST* sample. The graph corresponds to the vertically-averaged depth profile along the horizontal abscissa in the area highlighted by the dotted rectangle. Other profiles are given as supplementary material. From them, it is concluded that the surface of the horizontal bundles are lying some 8 μm above the vertical ones, themselves lying less than 10 μm above the octets, this last value being only approximate because of pores in the octets. These results are surprising because the vertical fiber bundles have been described as the most resistive phase [9]. Actually, measurements in vertical bundles are poorly accurate too, because only fiber tips can be seen by the microscope. Nevertheless, the effective recession rates seem very close to each other for all components except the thin interphase.

In figure 10, the profile of a horizontal fiber bundle across the composite surface is presented. It is clearly seen that these bundles have a wavy shape, which is probably due to composite manufacturing [6]: during the high-pressure pitch impregnation steps, the horizontal and vertical bundles are pressed against each other, therefore the section variations. Except this wavy pattern, the average surface height is constant throughout the sample. It can be concluded that the recession rate of the whole sample surface is constant. So, *ST* samples are good models for stagnation point recession. On the other hand, HS may give information about off-stagnation point recession rates.

Figure 11 shows relative height profiles (the heights are relative to the lowest

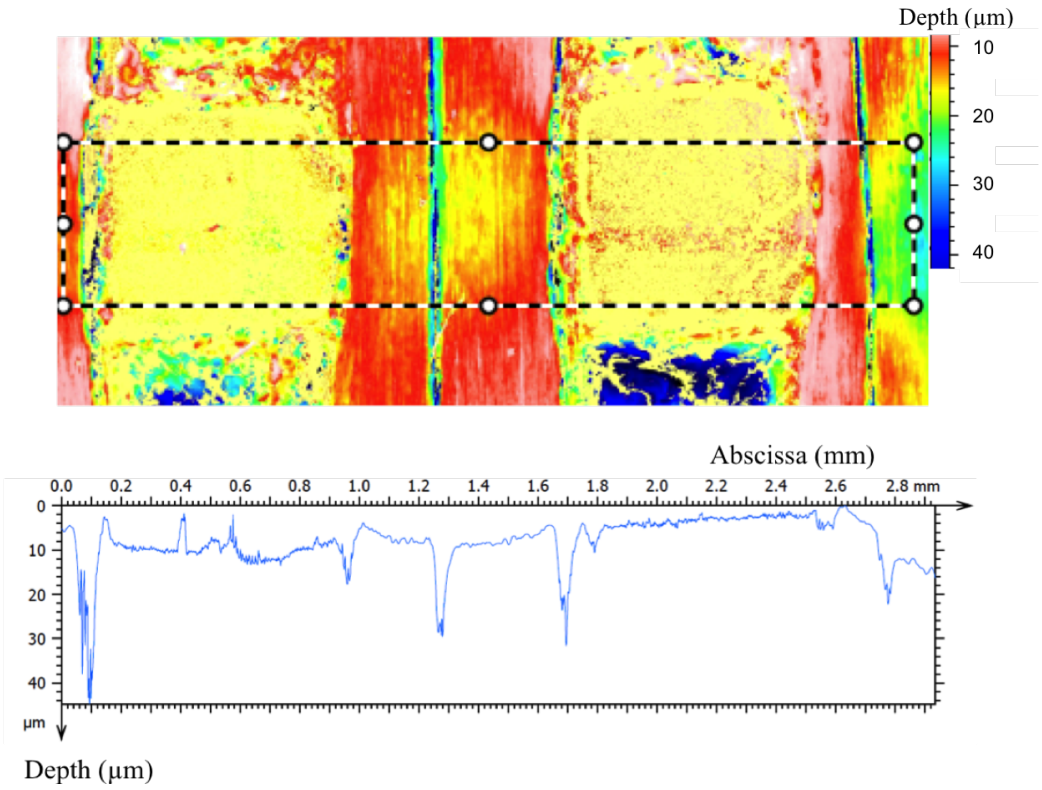

Figure 9: 3D profile and relative heights (relative to the highest point) measurements of *Reference ST* sample obtained by confocal microscopy.

point), measured from 3D profilometric data, of the center (stagnation point) (a), middle (b) and edge (c) of an HS sample ablated under air flow. For edge and stagnation point regions, the same results as for ST samples are found, with vertical bundles approximatively 10 µm below the horizontal ones. For the ”middle” region, the results are more difficult to interpret because the bundles have off-axis directions. But, as it is visible on Figure 11 c), all components have height differences are around 5 µm. Due to precision limitations, the interphase ablation depth cannot be measured on these pictures.

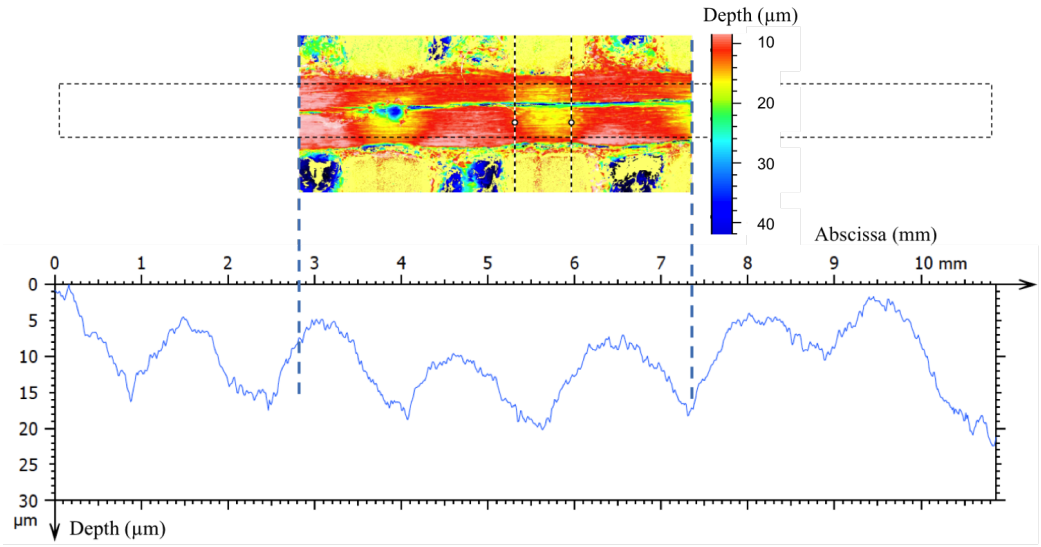

Figure 10: Height (relative to the highest point) of a horizontal bundle of fibers in *Oxidation ST* sample obtained by confocal microscopy

Figure 12 shows the relative heights of the interphase at the stagnation point for HS samples ablated under air and argon flows. In both cases, the interphases are deeply ablated with a depth of 113 µm for the oxidized sample and 48 µm for the sublimated one. The width of the ablated interphases is almost the same for both conditions (85 µm for the oxidized sample and 72 µm for the sublimated one). It should be noted that interphase ablated depth and width values are very scattered for the sublimated sample and that the measured values are probably upper bounds, due to the very low ablation rate and instrumental limitations.

All measurements of the final relative heights and interphase depth and width are summarized in table 5.

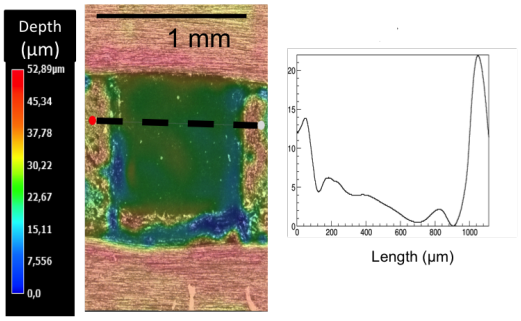

(a) center

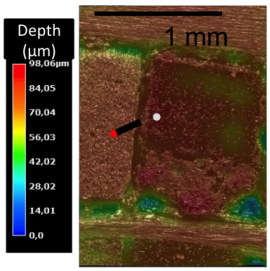

(b) middle

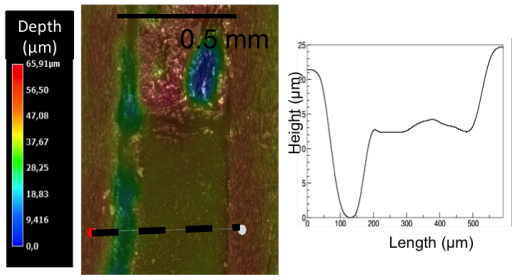

(c) edge

Figure 11: 3D measurements of relative heights (height relative to the lowest point of the studied zone) for *Oxidation HS* sample at three representative locations, obtained by digital microscopy. Locations are presented in Figure 6(a).

Case	HB|VB (µm)			VB|MO (µm)			Interface width (µm)			Interphase depth (µm)		
	Mean	σ	nb	Mean	σ	nb	Mean	σ	nb	Mean	σ	nb
Reference ST	< 5	-	-	14.4	5.9	14	93.2	27.1	7	17.1	7.8	7
Oxidation ST	11.2	1.8	8	9.3	5.9	14	77.6	15.9	11	30.6	7.1	11
Sublimation ST	20.2	1.4	16	-21	1.8	3	83	18.3	6	23.3	2.9	6
Oxidation HS	6.7	13.5	5	-19.1	7.5	3	105.3	15.2	3	115.1	15.6	3
Sublimation HS	8.3	3.5	2	-5.9	-	1	85.2	12.5	2	36.9	11.2	2

Table 5: Mean relative height and interface depth and width for five samples tested at VKI Plasmatron. Standard deviation and number of measures used for the average are also given. A positive value implies that the first component is higher than the second one and a negative value means the second component is higher than the first one. HB stands for Horizontal bundle, VB is Vertical Bundle and MO is Matrix Octet. σ is the standard deviation and 'nb' the number of measurement points.

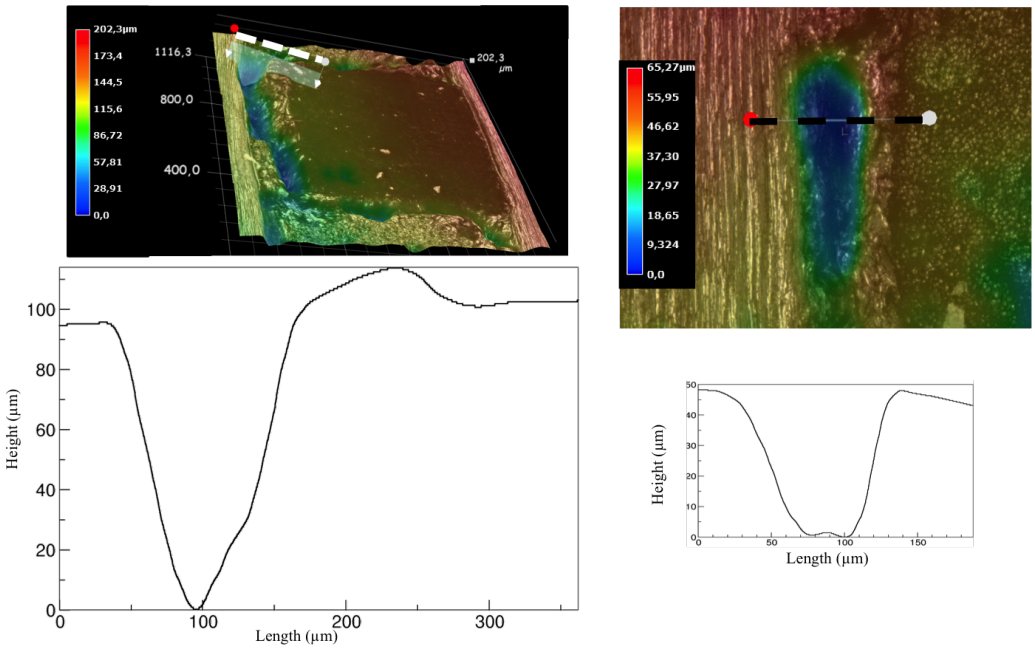

(a) *Oxidation ST* (b) *Sublimation ST*

Figure 12: Relative heights around interphases for *Oxidation ST* and *Sublimation ST* samples, obtained by digital microscopy.

4. Discussion

4.1. Epi-macro-structural roughness

At macroscopic scale, the vertical and horizontal fibers bundles and the matrix octets are the main components of the 3D C_f/C composite. Additionally, a thin interface (approximatively 20 µm) separates these components. The relative height of these components after ablation is governed on the one hand by the competition between surface reaction and gas species transfer, which depends on the fluid and on the material, and on the other hand on the reactivity ratios, which are only material characteristics and are defined as [28, 10, 9] :

$$A_{ij} = \frac{k_i \upsilon_i}{k_j \upsilon_j} \tag{3}$$

where k_i is the reaction rate and υ_i the molar volume of the i^{th} phase. Indeed, if the components have distinct surface reactivities, as far as gasification processes have an influence, height differences will appear. They will be maximal if diffusion above the surface is instantaneous. On the other hand, if diffusion above the surface become the only limiting process, then the reactivity differences do not play any role and the surface will not acquire roughness.

From the depth profiles, it is found that some reactivity gradients exist even inside a given macroscopic constituent. The fiber bundles look slightly more ablation-resistant on their periphery, i.e. close to the interphases, than in their center. The same occurs more markedly for the matrix octets, which contain a central pore. Figure 13 illustrates the consequence of such a reactivity gradient on the surface profile alteration, in the case of bundles. In addition, horizontal bundles have a wavy profile resulting from their processing history, as seen in figure 10.

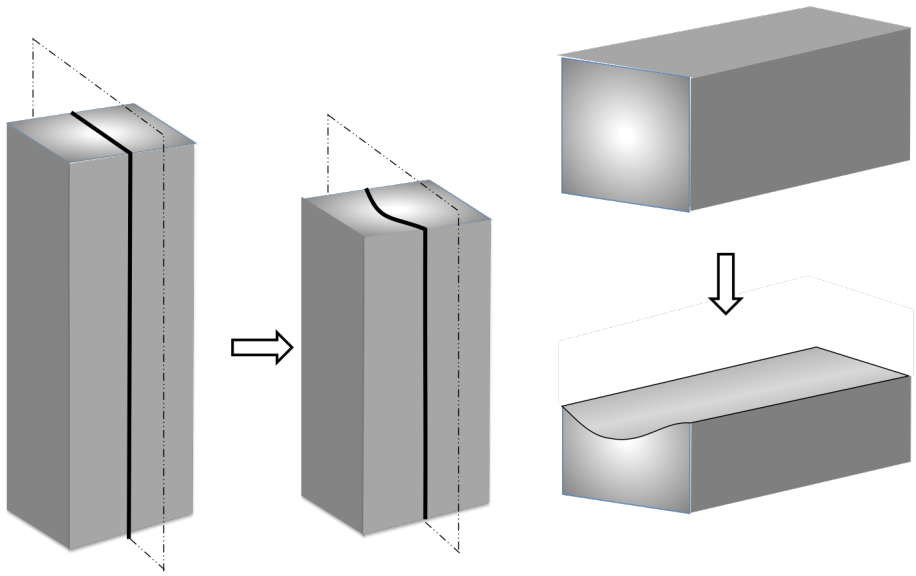

(a) Vertical bundles (b) Horizontal bundles

Figure 13: Schemes of bundles containing a softer central zone, before and after ablation

It becomes therefore much more difficult to define an average height for each constituting phase, especially for octets. Nonetheless, despite this appreciable uncertainty, we have identified (see Table 5) that horizontal bundles are more resistant than the vertical bundles, themselves slightly more resistant than the matrix octets (as far as average values can be determined for these more disorganized components).

The height differences are around only 20 µm for all components except for interphases which lie some 100 µm below the other components. Interfaces thicknesses are also quite large after ablation, with average values from 77 µm to 105 µm and their standard deviation is important due to the wide variety of interfaces coming from ablation of a less organized carbon between fibers bundles and matrix and pre-existing crack. Because thick grooves are better observed

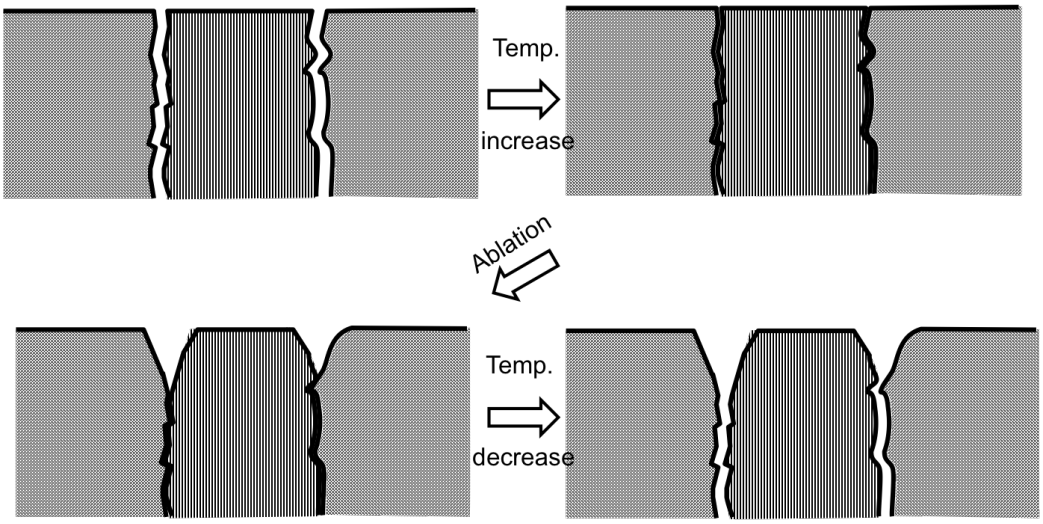

Figure 14: Schemes of the opening of composite interfaces during high temperature oxidation

by the microscope, these values may be overestimated. Nevertheless, interfaces width measurements have to be considered with caution because SEM and 3D images are taken at room temperature when ablation occurs at more than 2000 K and thermal expansion of fibers bundles may play a non-negligible role during ablation (Figure 14). When ablation of interface occurs, bundles can expand in the formed grooves.

Interface depth measurement for *ST* samples are not accurate because of limitations coming from the confocal microscope. Values less than 30 µm are at or below the optical limit of the microscope for our samples whereas values measured by digital microscopy are more trustworthy. Interface depth is around 100 µm which is 1/4 of the octet size.

HS samples allow comparisons between stagnation and off-stagnation points. Unfortunately, at the "middle" of samples, the pattern is too complicated and mea-

surements are too difficult to achieve. On the other hand, a few measurements could be done at the edge of samples, with values of the relative height of the horizontal bundles with respect to the vertical ones very close to the stagnation point for the *Oxidation HS* sample; however, the interphase ablation depth is smaller on the edge, denoting a lower ablation rate in this region. Conversely, sublimation rates, as inferred from the ablated interphase widths and depths, have been found equal on the edge and center of the *HS* samples.

4.2. Epi-micro-structural roughness

At micro scale, fibers in vertical bundles can have different shapes according to ablative conditions. As presented on figure 6, for an identical surface temperature, the fiber shape at the stagnation point is different for flat or hemispherical samples. On *HS* samples, the fibers acquire a needle shape (see section 3.2) but on the *ST* sample, the surface is smoother, with a three-zone pattern. Because the fiber diameter is under 10 μm the influence of gas flow between fibers is negligible at this scale and the fiber ablation is only driven by the oxygen diffusion/surface reaction ratio and the ablated tip shapes are determined by intra-fiber reactivity differences. So, we can infer that the fibers have an internal structure containing three zones: (*i*) a resistive core at the center, (*ii*) a slightly less resistive thin skin at the outer and (*iii*) an intermediate, neatly less resistive zone.

For sublimated sample, as evidenced in previous tests [9], the reactivity is reversed between fibers and intra-bundle matrix.

4.3. Diffusion/reaction competition analysis

During air flow ablation tests, it has been already shown that nitridation plays only a minor role in carbon removal [29, 30]. We also have checked that sublimation plays a minimal role in the chosen conditions. Because O is the dominant component in the plasma flow, it is the only species that need be taken into account for ablation of the composite. So, the major reaction is $C(s) + O(g) \longrightarrow CO(g)$. To explain the material behaviour under air, the main criterion is the balance between heterogeneous reaction and gas-phase diffusion of the oxidizing species through the boundary layer. The effective species diffusion coefficient D_i^{eff} of a multi-component mixture for species i are approximated by the following expression [31], which is also known as Blanc's law :

$$D_i^{eff} = \frac{1 - \chi_i}{\sum_{j \neq i} \frac{\chi_j}{D_{i,j}}} \tag{4}$$

where χ_i is the mole fraction of species i and $D_{i,j}$ is the mutual diffusion coefficient between species i and j. This coefficient is computed from reference [32]. The recession rate of the sample is calculated by the following equation :

$$\dot{r} = -\upsilon_s \mathbf{J} \cdot \mathbf{n} \tag{5}$$

where υ_s stands for the solid molar volume, $\mathbf{J}$ is the impinging flux of oxidizer and $\mathbf{n}$ the surface normal. The actual influence of the flow velocity is given by the Péclet number $Pé = \delta u_e / D_{O_e}$. In a first approximation, assuming a diffusion-limited regime with negligible convection ($Pé \ll 1$), the recession rate can be calculated by :

$$\dot{r}_{dl} = \frac{\upsilon_s D_{O_e} C_{O_e}}{\delta} \tag{6}$$

where D_{O_e} the diffusion coefficient of atomic oxygen calculated with values at the edge of the boundary layer, δ is the boundary layer thickness and C_{O_e} is

the concentration of oxygen at the same location. If convection were negligible, the experimental values $\dot{r}_{exp}$ should be lower than or equal to $\dot{r}_{dl}$. A comparison with measured recession rates are presented in table 6. The dimensionless ratio $\tilde{\dot{r}} = \dot{r}_{exp}/\dot{r}_{dl}$ has been calculated and is lying between 1 and 3, showing that convection cannot be neglected for the determination of the effective reaction rate, since it enhances the kinetics with respect to a diffusion-reaction only system. The values of Péclet numbers are given in table 6 and lie between 11 and 17 for all experiments. Figure 15 is a plot of the dimensionless rate against the Péclet number, showing a marked tendency to increase for the *ST* samples series. For the hemispherical sample, the value is higher for a lower Péclet number, which is due to the distinct flow structure in the latter case. This strongly supports the idea that convection has a direct influence on the concentration field of the oxidizing species and consequently on the ablation rate.

In addition, no mechanical erosion has been detected, since no flares were seen in the recorded movies.

Sample	δ (mm)	D_{O_e} $(m^2.s^{-1})$	C_{O_e} $(mol.m^{-3})$	$\dot{r}$ $(\mu m.s^{-1})$		*Pé*	$\tilde{\dot{r}}$
				$\dot{r}_{exp}$	$\dot{r}_{dl}$		
Reference ST	10	0.058	0.073	4.43	2.573	16	1.72
Long Duration ST	7.3	0.042	0.092	3.87	3.250	11	1.19
Oxidation ST	10	0.094	0.045	6.16	2.565	17	2.40
Oxidation HS	6.5	0.093	0.052	9.61	4.511	12	2.27

Table 6: Boundary layer edge conditions : oxygen diffusion coefficient (D_{O_e}), oxygen concentration (C_{O_e}) and boundary layer edge thickness (δ), including diffusion-limited (see eq. (6) (dl) and experimental (exp) recession rate and *Pé* number.

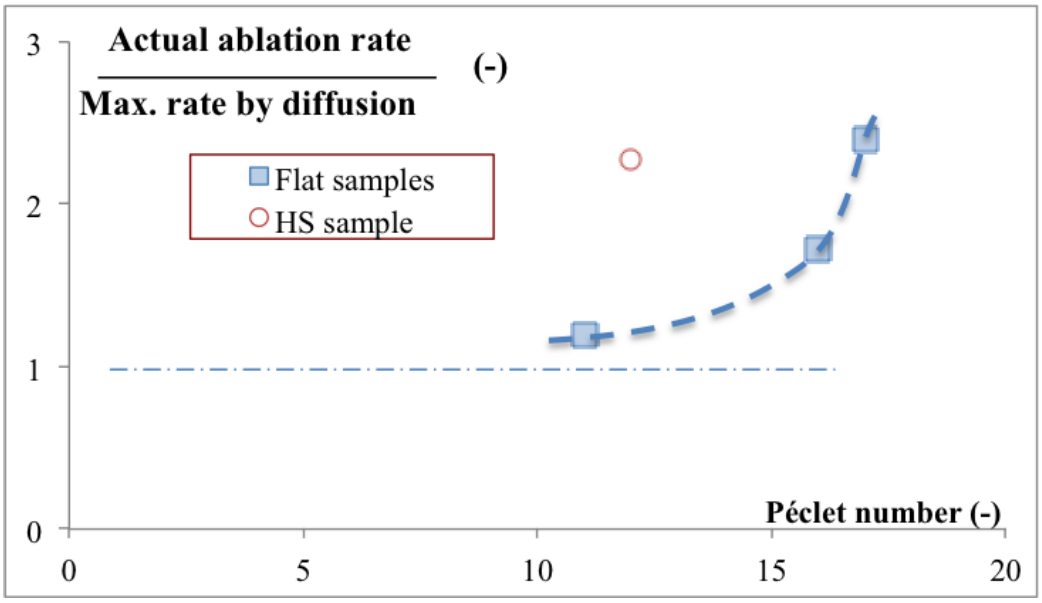

Figure 15: Recession rate scaled by the maximal rate $\tilde{r}$ obtained under the hypothesis of diffusional limitation as a function of *Pé* for all oxidation test cases.

Another point to mention is the following: the *Oxidation ST* sample has a much flatter steady-state morphology, as opposed to the *Oxidation HS* sample : this matches the fact that the species bulk transfer limitations are much larger in the former case, as illustrated in former works [10]. Indeed, this comes from the fact that the reaction rate is neatly faster for *Oxidation HS*: for this test, the total duration was enough for the sample to reach its steady state morphology, whereas it was not the case for the other one.

Though very encouraging, these results are preliminary.. This calls out for the development and exploitation of a more accurate model to retrieve the ablation properties of the 3D C_f/C composite.

5. Concluding remarks and perspective

Ablation experiments on flat and hemispherical samples of 3D C_f/C composites under air and argon plasmas have been carried out at the VKI Plasmatron facility. The surface temperatures were in range 2073 – 2806 K at test chamber pressure 1.5 kPa and 20 kPa. The plasma free stream condition, including temperature and mole fraction, was reconstructed by reactive fluid dynamics computations. The recession rate was measured by three different methods : one in-situ and two post-test methods. It was found very low for sublimated samples – often under the resolution limit of the methods. SEM micrographs of all cases were taken and patterns commonly observed at macro- and micro-scale were found. Confocal microscopy and 3D digital microscopy were used to provide a three-dimensional view of the ablated samples surfaces.

There was a very small height difference between fibers bundles and matrix octet; horizontal fibers bundles resist slightly better than vertical bundles. Interphases, coming from a less organized carbon and containing pre-existing cracks, were measured whenever possible and their depth was approximatively $1/4$ of a matrix octet height or bundle edge size. An inhomogeneous reactivity of fibers bundles was pointed out by these macroscopic results: a slight reactivity gradient coming from the edge to the center of bundles and octets was found.

At micro scale, *ST* samples under air flow reveal the internal structure of the carbon fiber which is separated in three distinct zones : a resistive core, a weaker intermediate zone, and a thin resistive skin. This pattern was not seen on *HS* samples where only a simple needle tip shape stays visible. The reactivity contrast between fibers and intra-bundle matrix was not the same in oxidation or sublimation: the fibers are more resistant to oxidation but the matrix is more resistant to

sublimation.

Thanks to the numerically reconstructed concentration fields, the respective role of diffusion, convection and heterogeneous reaction has been clarified. At the macroscale, convection is never negligible and increases the recession rate with respect to what pure diffusion would give. The diffusion/reaction ratio has been evaluated, showing in all cases a neat limitation of the overall recession kinetics by mass transfer, which was expected from the high values of the surface temperatures. At the microscale, it has been found that the reaction/diffusion ratio has an important impact on the steady surface morphology, as anticipated in previous analytical studies [10, 33].

These results encourage to perform detailed simulation of the surface evolution under the simultaneous action of diffusion, convection and heterogeneous reaction – this is currently under way, thanks to evolutions of the AMA simulation software [34]. This numerical model will also have to take into account reactivity contrast (or gradients) inside bundles, as well as anisotropic reactivity. Finally, another forthcoming research direction is to better investigate experimentally the effect of pure sublimation, going to higher temperatures and flow rates in order to obtain larger ablation rates, and comparing the results with ablation under air.

Acknowledgements

The authors wish to acknowledge CEA for financial support to C. Levet under the form of a Ph.D. grant. The Plasmatron facility was operated by P. Collin. VKI ICP calculations were performed by Z. Alsalihi. Confocal microscopy data was obtained at PACEA lab with the kind assistance of A. Queffélec and 3D digital microscopy was achieved at CEA Le Ripault with the help of T. Le Bihan.

References

[1] G. Savage. *Carbon/Carbon Composites*. Chapman & Hall, 1993.

[2] G. Duffa. *Ablative Thermal Protection Systems Modeling*. AIAA Education Series. AIAA, New York, NY, 2013.

[3] J. Couzi, J. de Winne, and B. Leroy. Improvements in ablation predictions for reentry vehicle nosetip. In *Procs. 3rd European Symposium on Aerothermodynamics for Space Vehicles*, R.A. Harris, ed., *ESA Conf. Procs.*, SP-426, 493–499, ESA, Noordwijk, The Netherlands, 1998.

[4] K. Kuo and S. Keswani. A comprehensive theoretical model for carbon-carbon composite nozzle recession. *Combustion Science and Technology*, 42(3-4):145–164, 1985.

[5] V. Borie, J. Brulard, and G. Lengellé. Aerothermochemical analysis of carbon-carbon nozzle regression in solid-propellant rocket motors. *Journal of Propulsion and Power*, 5(6):665–673, 1989.

[6] E. Fitzer and L. M. Manocha. *Carbon Reinforcements and Carbon/Carbon Composites*. Springer, Berlin Heidelberg, 1998.

[7] S. Pestchanyi, V. Safronov, and I. Landman. Estimation of carbon fibre composites as ITER divertor armour. In *Procs. 11th Intl. Conf. on Fusion Reactor Materials (ICFRM-11). Journal of Nuclear Materials*, 329-333(A):697 – 701, 2004.

[8] D. M. Duffy. Fusion power materials. *Advanced Materials and Processes*, 168(7):15–18, 2010.

[9] G. L. Vignoles, J. Lachaud, and Y. Aspa. chapter 12 : Environmental Effects: Ablation of C/C materials - surface dynamics and effective reactivity, pages 353–384. In *Ceramic Matrix Composites: Materials, Modeling and Technology*, N. Bansal and J. Lamon eds., J. Wiley & Sons, Hoboken, NJ, 2014.

[10] G. L. Vignoles, J. Lachaud, Y. Aspa, and J.-M. Goyhénèche. Ablation of carbon-based materials: multiscale roughness modelling. *Composites Science and Technology*, 69(9):1470–1477, 2009.

[11] J. Lachaud, G. L. Vignoles, J.-M. Goyhénèche, and J.-F. Epherre. Ablation in C/C composites: microscopic observations and 3D numerical simulation of surface roughness evolution. In *Procs. 6^{th} Pacific Rim Conference on Ceramic and Glass Technology (PacRim6)*,M. Affatigato, editor, *Ceram. Trans.* 191, 149–160, The American Ceramic Society, Westerville, OH, 2006.

[12] D. C. Reda. Correlation of nosetip boundary layer transition data measured in ballistic range experiments. Technical Report SAND 790649, Sandia National Laboratories, Livermore, CA, 1979.

[13] R. G. Batt and H. H. Legner. A review of roughness-induced nosetip transition. *AIAA Journal*, 21(1):7–22, 1983.

[14] M. R. Wool. Summary of experimental and analytical results. Technical Report SAMSO-TR-74-86, Passive Nosetip Technology Program (PANT), January 1975.

[15] B. Bottin, M. Carbonaro, V. Van Der Haegen, and S. Paris. Predicted and measured capability of the 1.2 MW plasmatron regarding re-entry simula-

tion. In *Proceedings of the 3rd European Symposium on Aerothermodynamics for space vehicles*,R. A. Harris, editor, *ESA Conf. Procs.* SP-426, 553–560, ESA Publications, Noordwijk, The Netherlands, 1998.

[16] B. Bottin, O. Chazot, M. Carbonaro, V. Van Der Haegen, and S. Paris. The VKI plasmatron characteristics and performance. In *Measurement Techniques for High Enthalpy and Plasma Flows*, volume RTO-EN-8 of *Research and Technology Organization Educational Notes*, pages 6–1 – 6–26, Rhode-Saint-Genèse (Belgium), 1999. NATO.

[17] A. F. Kolesnikov. Conditions of simulation of stagnation point heat transfer from a high-enthalpy flow. *Fluid Dynamics*, 28(1):131–137, 1993.

[18] G. Degrez, D. Vanden Abeele, P. Barbante, and B. Bottin. Numerical simulation of inductively coupled plasma flows under chemical non-equilibrium. *International Journal of Numerical Methods for Heat & Fluid Flow*, 14(4):538–558, 2004.

[19] D. Vanden Abeele and G. Degrez. Efficient computational model for inductive plasma flows. *AIAA Journal*, 38(2):234–242, 2000.

[20] T. E. Magin and G. Degrez. Transport algorithms for partially ionized and unmagnetized plasmas. *Journal of Computational Physics*, 198(2):424 – 449, 2004.

[21] J. B. Scoggins and T. E. Magin. Development of Mutation++: Multicomponent Thermodynamic and Transport Properties for Ionized Plasmas written in C++. In *Procs. 11th AIAA/ASME Joint Thermophysics and Heat Transfer Conference*, Atlanta, GA, 2014. AIAA.

[22] E. Duvivier, R. Naslain, R. Pailler, S. Labruquere, and X. Bourrat. The role of interfaces in the oxidation of 3D-carbon/carbon composites. In *Procs. 26th Annual Conference on Composites Advanced Ceramics Materials and Structures : A*, H.-T. Lin and M. Singh, eds., *Ceramics Engineering & Science Proceedings* 23, 287–294, The American Ceramic Society Westerville, OH, 2002.

[23] E. Duvivier. *Cinétique d oxydation d'un composite carbone/carbone et influence sur le comportement mécanique*. PhD thesis, University of Bordeaux I, 1997. In French.

[24] D.-W. Cho and B.-I. Yoon. Microstructural interpretation of the effect of various matrices on the ablation properties of carbon-fiber-reinforced composites. *Composites Science and Technology*, 61(2):271 – 280, 2001.

[25] J.C. Han, X.D. He, and S.Y. Du. Oxidation and ablation of 3D carbon-carbon composite at up to 3000 °C. *Carbon*, 33(4):473 – 478, 1995.

[26] Y.-J. Lee and H.-J. Joo. Investigation on ablation behavior of CFRC composites prepared at different pressures. *Composites Part A: Applied Science and Manufacturing*, 35(11):1285 – 1290, 2004.

[27] J. Lachaud, G. L. Vignoles, V. Ducamp, J.-F Epherre, J.-M Goyhénéche, G. Duffa, and B. Vancrayenest. A new experimental/theoretical approach to measure and extrapolate the ablative properties of TPS materials. In *Procs. 5th ESA International Planetary Probe Workshop*, Bordeaux, France, J.-M. Bouilly, editor, ESA/ARA, 2007.

[28] Jean Lachaud, Yvan Aspa, and Gerard L. Vignoles. Analytical modeling of the steady state ablation of a 3D C/C composite. *International Journal of Heat and Mass Transfer*, 51:2614–2627, 2008.

[29] B. Helber, A. Turchi, O. Chazot, and T. Magin. Physico-chemistry of CN in the boundary layer of graphite in nitrogen plasma. In *45th AIAA Thermophysics Conference*, *AIAA Paper* 2015-2668, 2015.

[30] C. Park. *Nonequilibrium hypersonic aerothermodynamics*. John Wiley & Sons, New York, NY, 1990.

[31] K. Sutton and P. A. Gnoffo. Multi-component diffusion with application to computational aerothermodynamics. In *Procs. 7^{th} AIAA/ASME joint thermophysics and heat transfer conference*, Albuquerque (US-NM), 1998, AIAA Paper no. 98-2575.

[32] J.M. Yos. Transport properties of nitrogen, hydrogen oxygen, and air to 30,000K. Technical memorandum RAD-TM-63-7, Research and advanced development division AVCO corporation, 1963.

[33] G.L. Vignoles, J. Lachaud, Y. Aspa, and M. Quintard. Effective surface recession laws for the physico-chemical ablation of C/C composite materials. In *Mechanical Properties and Performance of Engineering Ceramics and Composites V - Procs. 34^{th} International Conference on Advanced Ceramics and Composites, ICACC'10*, D. Singh and J. Salem, eds., *Ceramics Engineering & Science Proceedings* 31(2), 351–360, The American Ceramic Society, Wiley, New York, 2010.

[34] J. Lachaud, Y. Aspa, and G. L. Vignoles. A brownian motion simulation technique to simulate gasification and its application to ablation. *Computational Materials Science*, 44:1034–1041, 2009.

AppendixA. Supplementary Material

AppendixA.1. Additional surface profiles of sample Reference ST

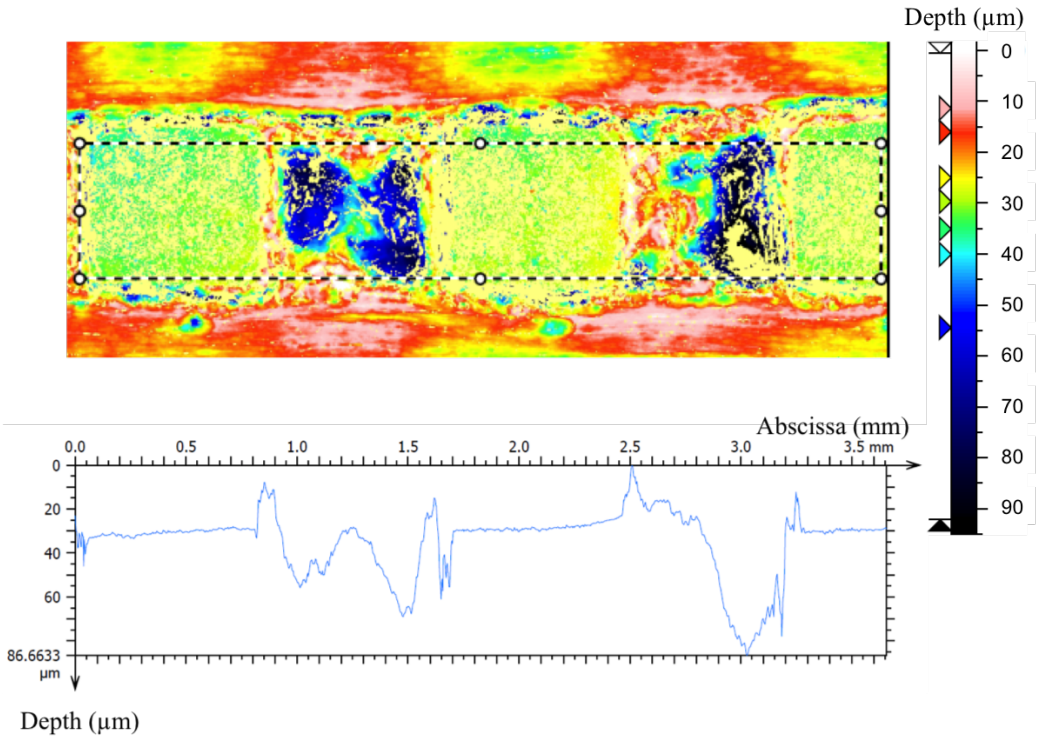

Figure A.16: 3D profile and relative heights measurements of sample *Reference ST* using confocal microscopy

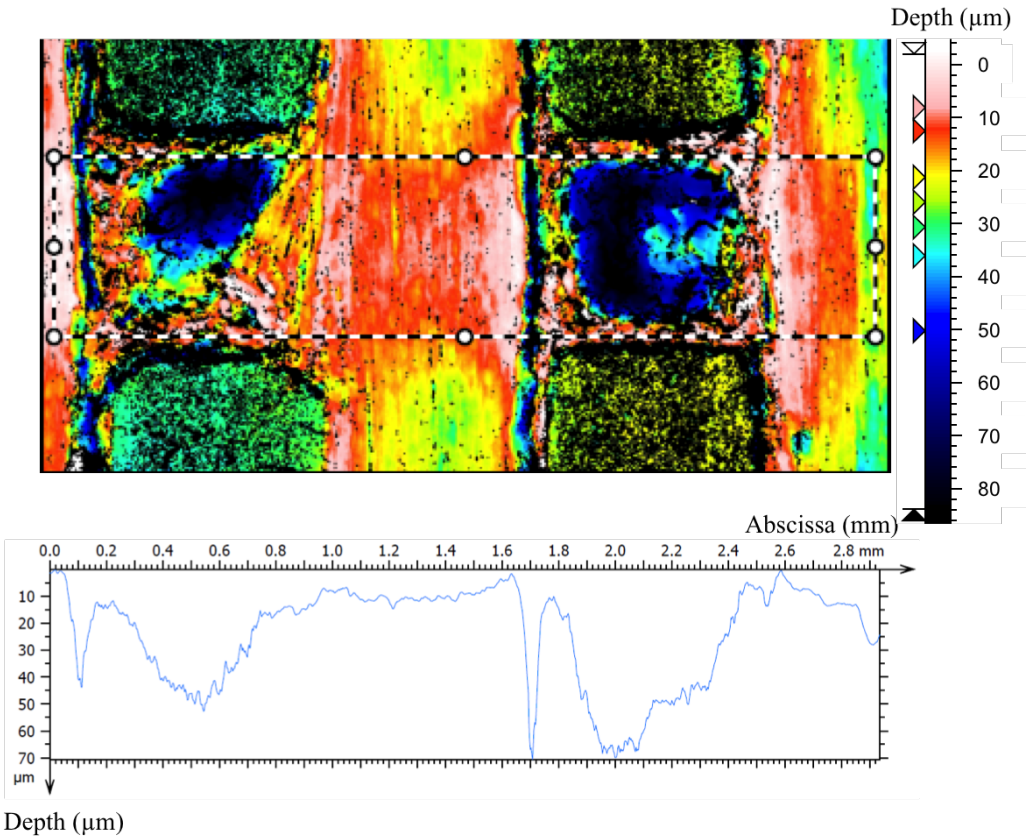

Figure A.17: 3D profile and relative heights measurements of sample *Reference ST* using confocal microscopy